

Quarterly Progress Report

N01-NS-1-2333

Restoration of Hand and Arm Function by Functional Neuromuscular Stimulation

Period covered: July 1, 2005 to September 30, 2005

Principal Investigator: Robert F. Kirsch, Ph.D.

Co-Investigators:

Patrick E. Crago, Ph.D.
P. Hunter Peckham, Ph.D.
J. Thomas Mortimer, Ph.D.
Kevin L. Kilgore, Ph.D.
Michael W. Keith, M.D.
David L. Wilson, Ph.D.
Dawn Taylor, Ph.D.

Joseph M. Mansour, Ph.D.
Jeffrey L. Duerk, Ph.D.
Wyatt S. Newman, Ph.D.
Harry Hoyen, M.D.
John Chae, M.D.
Dustin Tyler, Ph.D.

Program Manager: William D. Memberg, M.S.

Case Western Reserve University
Wickenden 407
10900 Euclid Avenue
Cleveland, OH 44106-7207
216-368-3158 (voice)
216-368-4969 (FAX)
rfk3@po.cwru.edu

Contract abstract

The overall goal of this contract is to provide virtually all individuals with a cervical level spinal cord injury, regardless of injury level and extent, with the opportunity to gain additional useful function through the use of FNS and complementary surgical techniques. Specifically, we will expand our applications to include individuals with high tetraplegia (C1-C4), low tetraplegia (C7), and incomplete injuries. We will also extend and enhance the performance provided to the existing C5-C6 group by using improved electrode technology for some muscles and by combining several upper extremity functions into a single neuroprosthesis. The new technologies that we will develop and implement in this proposal are: the use of nerve cuffs for complete activation in high tetraplegia, the use of current steering in nerve cuffs, imaging-based assessment of maximum muscle forces, denervation, and volume activated by electrodes, multiple degree-of-freedom control, the use of dual implants, new neurotization surgeries for the reversal of denervation, new muscle transfer surgeries for high tetraplegia, and an improved forward dynamic model of the shoulder and elbow. During this contract period, all proposed neuroprostheses will come to fruition as clinically deployed and fully evaluated demonstrations.

Summary of activities during this reporting period

The following activities are described in this report:

- *Surgical implantation of nerve cuff electrodes*
- *Percutaneous evaluation of nerve cuff electrodes in high tetraplegia*
- *Feed-forward control of neuroprosthetic systems characterized by redundant muscles acting on multiple degrees of freedom*
- *Real-time EEG control of virtual cursor/arm movements*

Surgical implantation of nerve cuff electrodes

Contract sections: E.1.a.vi.4.3 Implementation of neuroprostheses for high tetraplegia
E.2.a.ii.4.3 Implementation of advanced upper extremity neuroprosthesis

Summary

In this quarter, four nerve cuff electrodes were successfully implanted in the upper extremity and trunk of a subject with high cervical level tetraplegia. The electrode leads were connected to temporary percutaneous leads to allow the nerve cuff electrodes to be studied. A second nerve cuff electrode implantation surgery that had been scheduled for this quarter in a subject with C5/C6 level tetraplegia was postponed for medical and personal reasons, and has been rescheduled for the next quarter.

Methods

"High Tetraplegia" neuroprosthesis candidate

As stated in the previous quarter's progress report, the candidate selected for this study is a 48-year-old African-American female who sustained a hemisection of the spinal cord at the C1-C2 level from a gunshot wound in 1994. Her right upper extremity is totally paralyzed, while

her left upper extremity has diminished, but functional use. She has diminished sensation in her right upper extremity, with some pain hypersensitivity. She also has diminished movement of her lower extremities, being able to stand for short periods, but not walk. Due to the high level of her injury, there was little to no denervation of the upper extremity nerves that we tested, so that all the muscles of interest were able to be electrically activated. This candidate has had far fewer secondary health complications than individuals with complete high-level spinal cord injuries tend to have. Her muscle excitability, health status, and interest in participating in this research study make her an excellent candidate.

In the first phase of the neuroprosthesis implantation, four nerve cuff electrodes were implanted, with the leads connected to percutaneous wires for external testing. The four nerves implemented were selected based on previous work in this Contract, including cadaver studies and simulations performed with a model of the shoulder. These four nerves are:

- Radial nerve – four contacts on the cuff could allow selective control of elbow extension, wrist extension, and finger extension.
- Musculocutaneous nerve – four contacts on the cuff could allow selective control of elbow flexion and forearm supination (biceps, brachialis).
- Axillary nerve – whole nerve stimulation for arm elevation (deltoid).
- Suprascapular nerve – whole nerve stimulation for stabilizing the rotator cuff capsule and humeral rotation (supraspinatus, infraspinatus).

Results

Axillary nerve

The axillary nerve was exposed and tested with a bipolar probe. The nerve diameter was measured at 4 mm, so a 4 mm diameter nerve cuff electrode was selected. The nerve cuff

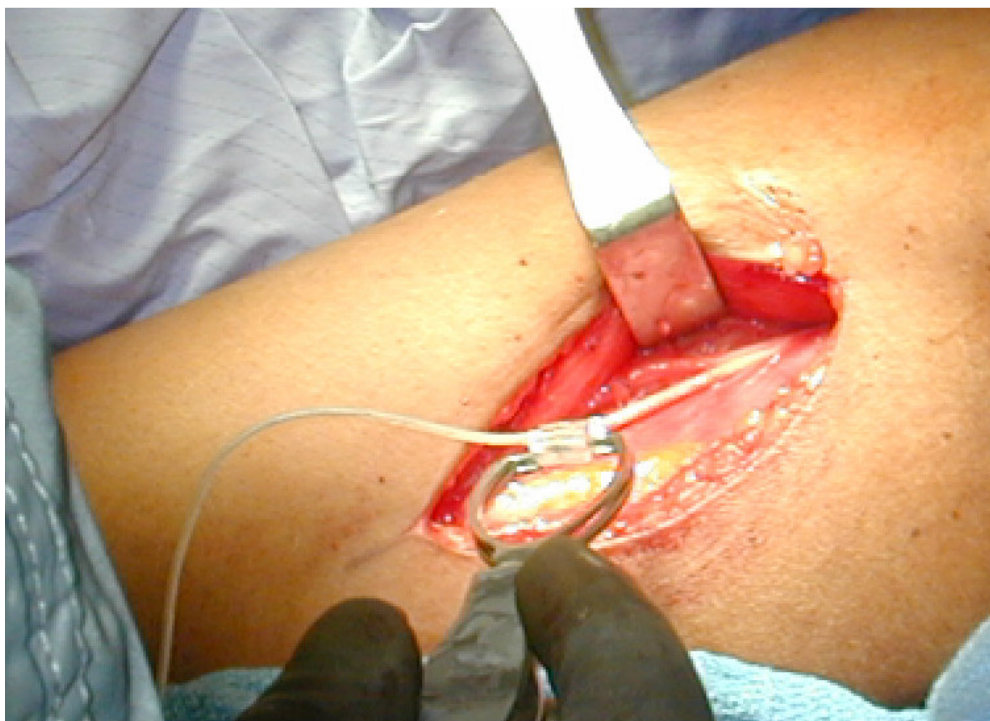


Figure 1. Nerve cuff electrode being held by a double-hooked forceps prior to being placed around the musculocutaneous nerve.

electrode was placed on a custom-designed double-hooked forceps (Figure 1) to facilitate wrapping the cuff around the nerve. The electrode was placed on the nerve and tested (see Figure 2). Appropriate activation of the deltoid muscles was achieved.

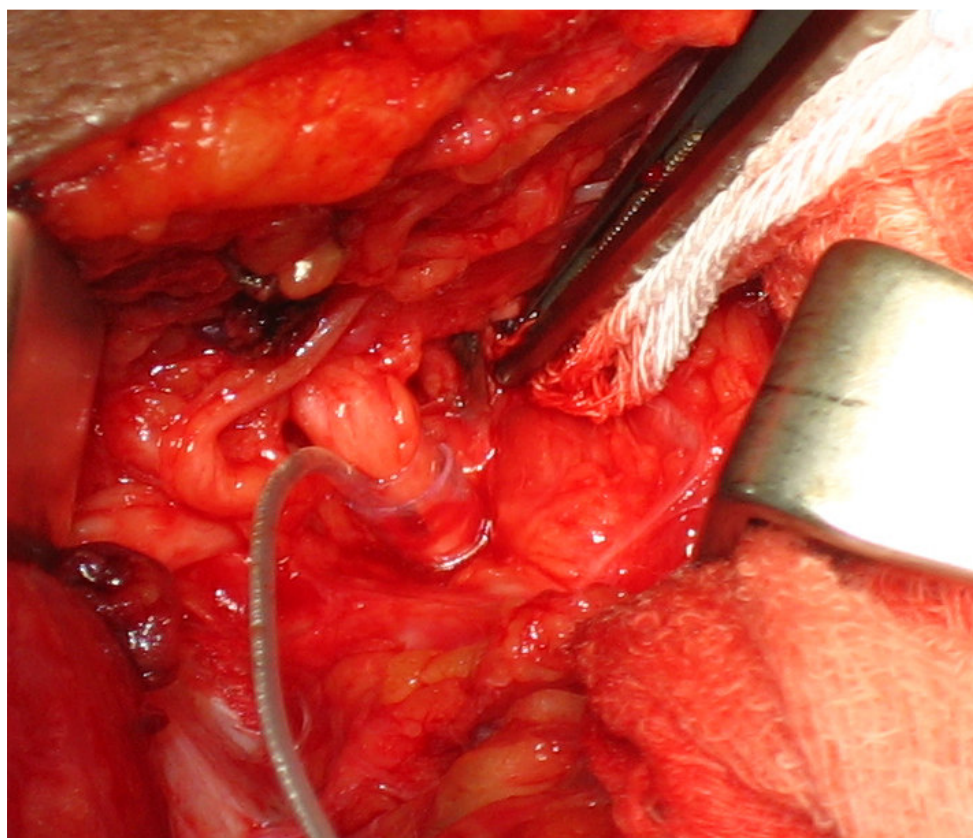


Figure 2. Nerve cuff electrode placed around the axillary nerve.

Radial nerve

The radial nerve was exposed near the location where the nerve branches to the long head of the triceps. The nerve diameter was measured at 6 mm. We wanted to investigate whether the different contacts of the cuff electrode could selectively activate different portions of the radial nerve, so a 6 mm diameter, four-lead electrode was selected (one lead for each contact). We wanted to avoid stimulating the long head of the triceps (since it adducts the shoulder), so the cuff electrode was placed distal to the long head branch. The electrode was tested by stimulating each contact. Selective activation was observed, since one contact activated triceps without activating wrist extension. One of the contacts appeared to have a high impedance, so the electrode was removed and tested. All four contacts were functional, so the impedance was attributed to an air bubble over the contact. The contacts were flushed with sterile saline and the electrode was placed back on the radial nerve at the same location as before. Each contact was stimulated again and all four contacts were functional. Selective activation of the triceps was observed again.

Suprascapular nerve

The suprascapular nerve was exposed and tested with the probe. The nerve diameter was measured at 3 mm, so a 3 mm diameter nerve cuff electrode was selected. The electrode was

placed on the nerve and tested (see Figure 3). Appropriate activation of the infraspinatus and supraspinatus muscles was achieved.

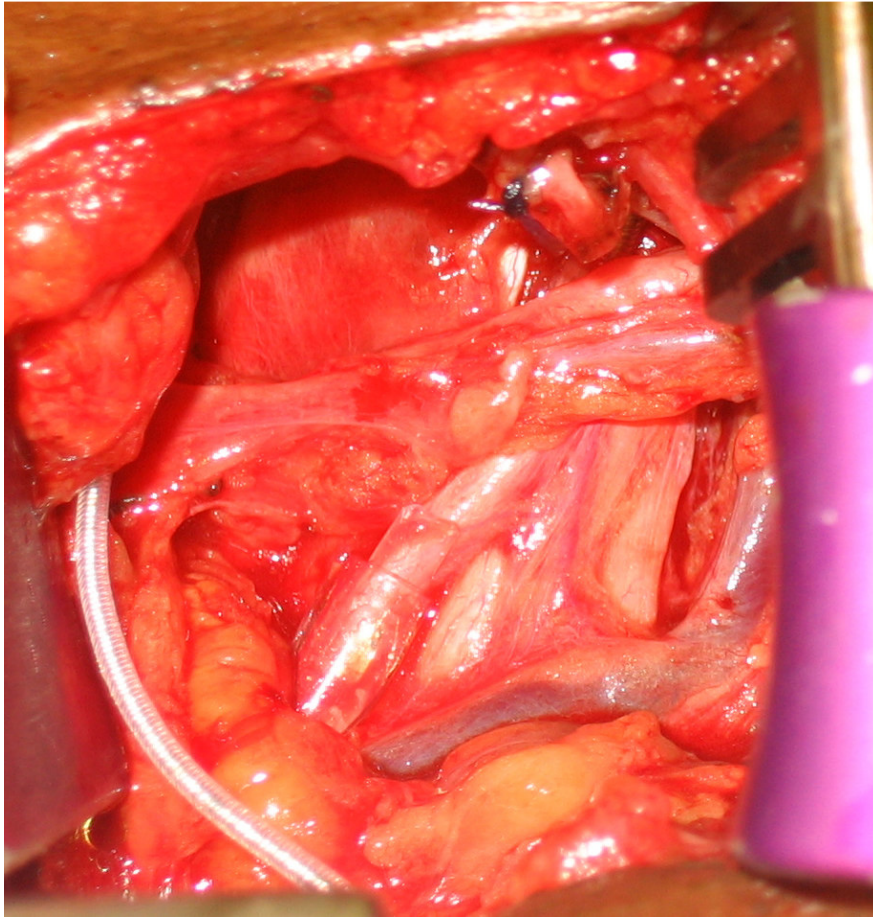


Figure 3. Nerve cuff electrode placed around the suprascapular nerve.

Musculocutaneous nerve

The musculocutaneous nerve was exposed and tested with the probe (see Figure 1). The nerve diameter was measured at 3 mm. Since we wanted to also investigate selective activation on this nerve, a four-lead electrode was selected. The smallest diameter four-lead electrode that we had available was a 4 mm diameter one, so we selected that one. The electrode was placed on the nerve and tested. Appropriate activation of the elbow flexors was observed, but we could not determine if the biceps and brachialis were being activated selectively with different contacts.

Tunneling leads and percutaneous connections

The leads from all four cuff electrodes were tunneled to a site in the abdomen just under the ribs near where the stimulator will be placed. A connector incision was made, and each lead was connected to a percutaneous lead adapter. Each percutaneous lead was passed via an angiocath through the skin at a location lateral to the connector site. After each percutaneous lead was tested to show electrical continuity to the cuff electrode, all the incisions were closed.

Post-surgical care

The incision sites were bandaged and the shoulder was stabilized with a velpeau restrictive dressing. X-rays were taken of the arm and shoulder (see Figure 4). Pins were crimped onto the percutaneous leads and placed into connector blocks so that cables could easily be plugged into the leads (see Figure 5). The exit site between the two connector blocks was covered with a bandage. The shoulder was stabilized for 3 weeks, after which the electrodes were characterized and exercise stimulation patterns were started.



Figure 4. X-ray showing 3 of the 4 nerve cuff electrodes.



Figure 5. Percutaneous leads in connector blocks.

Percutaneous Evaluation of Nerve Cuff Electrodes in High Tetraplegia

Contract section:

E.1.a.i.4.4. Evaluation of single and multicontact cuffs via percutaneous leads

Methods

Implant: Four percutaneous spiral nerve cuff electrodes were implanted in one subject with high cervical spinal cord injury. Four channel electrodes (Figure 6B) were implanted on the radial and musculocutaneous nerves and single channel electrodes (Figure 6A) were implanted on the suprascapular and axillary nerves (Figure 6). During the implant surgery, recruitment curves were generated by stimulating each contact and recording the EMG signals using needle EMG recording electrodes. Following the implant, the subject's arm was immobilized for three weeks with a sling and swab to allow for electrode encapsulation.

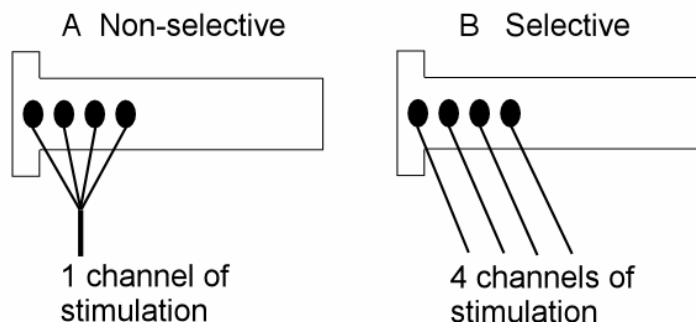


Figure 6. Schematic of non-selective and selective electrodes. Non-selective electrodes have all four contacts tied together, resulting in a single channel of stimulation. Selective electrodes have four individually controlled contacts, resulting in four channels of stimulation.

Exercise: Following the three week immobilization period, threshold and supramaximal activation values were determined for each electrode to verify muscle contraction and establish an exercise regime. During this first stimulation session, the current intensity was slowly increased for each channel of each electrode. Once the threshold and maximum values were determined, an exercise pattern was set-up that cycled stimulation between the shoulder and the arm. The axillary and the suprascapular nerves were stimulated together, and the radial and musculocutaneous nerve were alternated. The subject was instructed to exercise at home for two hours a day.

Moment Measurements: Tetanic stimulation (12.5 Hz) was used to measure the force production capabilities of the muscles at 7 and 9 weeks post implant. To measure shoulder moments, the subject was placed in a setup consisting of a JR3 force and moment transducer attached to the endpoint of the humerus with the elbow bent to 90°. The shoulder was position at 45° of abduction and 0° of horizontal flexion. To measure elbow, wrist, and finger moments, the subject was placed in a device consisted of 4 individual four bar linkage transducers, one for the elbow and wrist and one for each of the first two fingers (see Figure 7).

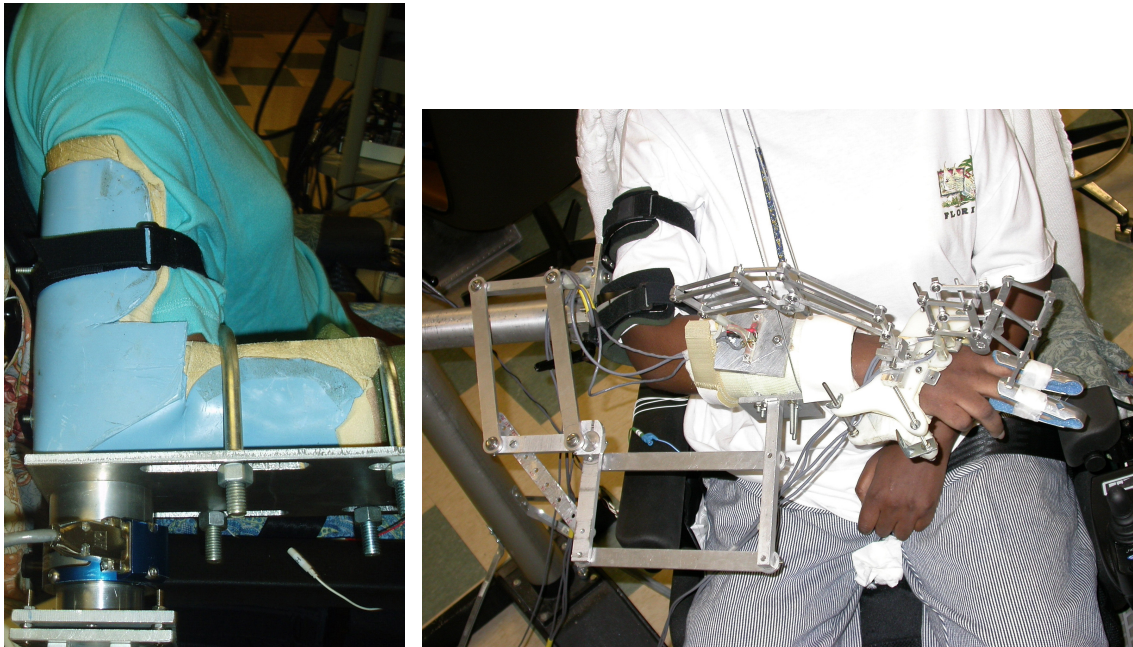


Figure 7. Pictures of moment measurement devices. Left – JR3 mounted at the end of the humerus to measure shoulder moments. Right - Four bar linkages used to measure moments at elbow, wrist and the first 2 fingers.

Electromyography Recordings: Surface and percutaneous EMG recordings were used to evaluate recruitment and selectivity of each nerve. Twitch recruitment curves were generated using both monopolar stimulation and current steering (simultaneous, subthreshold activation of adjacent contacts). Surface EMG recruitment was recorded at 5 weeks post implant to evaluate the stability of the electrodes and have baseline values. Because of the accuracy required to evaluate selective activation, percutaneous EMG recordings were obtained 8 weeks post implant from the musculocutaneous nerve. Evaluation of radial nerve selectivity is scheduled for a future test session.

Results

Sensation: The subject could feel the stimulation and reported that it felt like a muscle massage. As stimulation was increased, the sensation spread to other portions of the forearm that corresponded to the appropriate dermatomes for the stimulated nerve. Between threshold and supramaximal motor stimulation, the subject did not report any painful sensations. If the stimulation levels were increased significantly beyond supramaximal, the subject would report a painful sensation.

Electrode Positional Stability: To determine if the electrodes move during and after the surgery, the recruitment curves generated intraoperatively were compared with curves generated 5 weeks post implant (Figure 8). At both times, stimulation of channel 1 resulted in triceps activation before the other muscles while stimulation of channel 3 resulted in activation of triceps last. Qualitatively, the selectivity appears to have improved following electrode encapsulation. This indicates that intraoperative testing is a valid predictor of chronic performance.

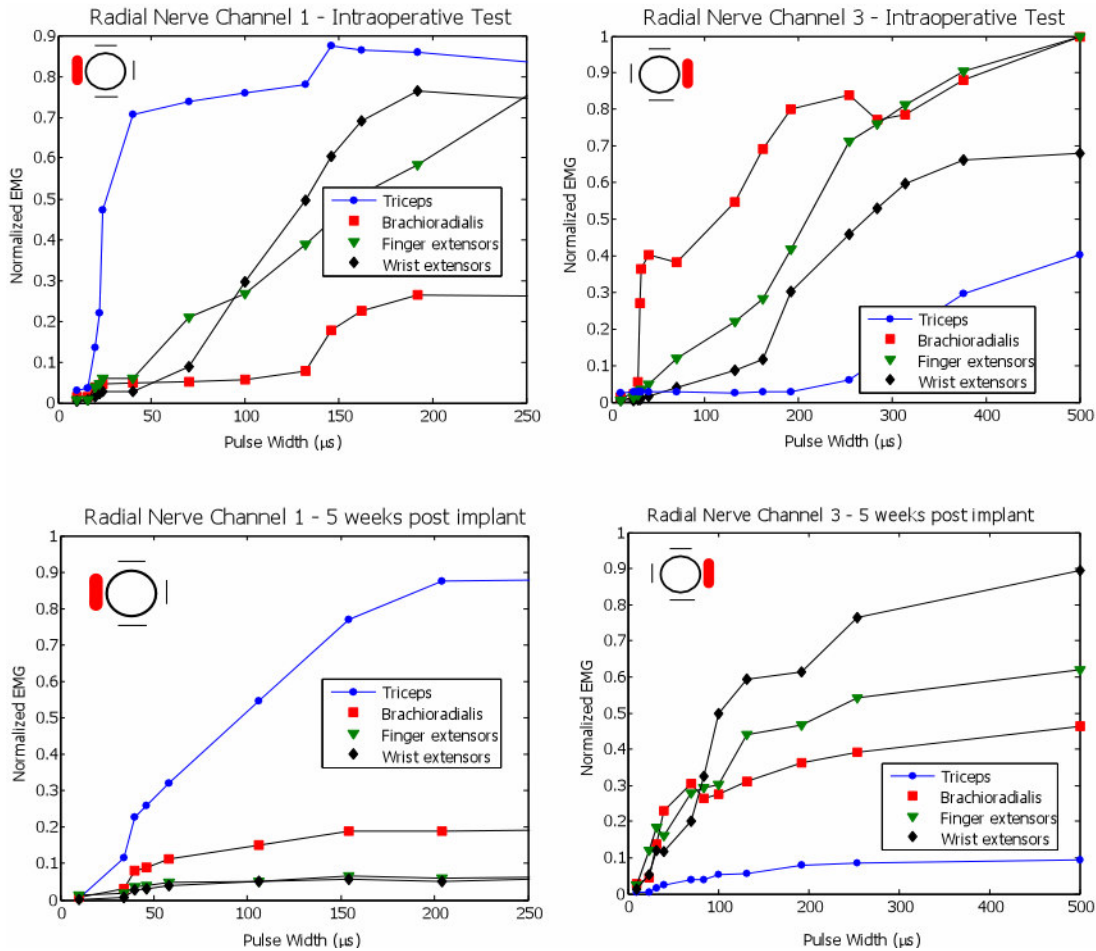


Figure 8: Comparison of radial nerve electrode selectivity 5 weeks post implant to the selectivity recorded during the implant surgery. The schematic in the upper left hand corner of each plot visually depicts the channel used for stimulation. Channel 1 activates triceps first in both cases and channel 3 activates triceps last in both cases.

Thresholds: The average threshold at 5 weeks post implant was 27 nC. This is significantly lower than the 420 nC required for threshold activation of the triceps using muscle electrodes (Kilgore et al., 2003). This lower threshold greatly reduces the power requirements of an implanted nerve stimulator.

Selective Activation: Monopolar cathodic stimulation selectively activated the triceps on the radial nerve (Figure 8) but was not capable of selectively activating the biceps or the brachialis on the musculocutaneous nerve. Current steering (simultaneous subthreshold anodic stimulation of adjacent contacts) improved the musculocutaneous nerve selectivity (Figure 9) and has yet to be attempted on the radial nerve. On the musculocutaneous nerve, stimulation of channel 1 with current steering on channel 2 activated 70% of brachialis before biceps reached 20% activation. Stimulation of channel 3 with current steering on channel 1 activated 70% of biceps before brachialis reached 30% activation.

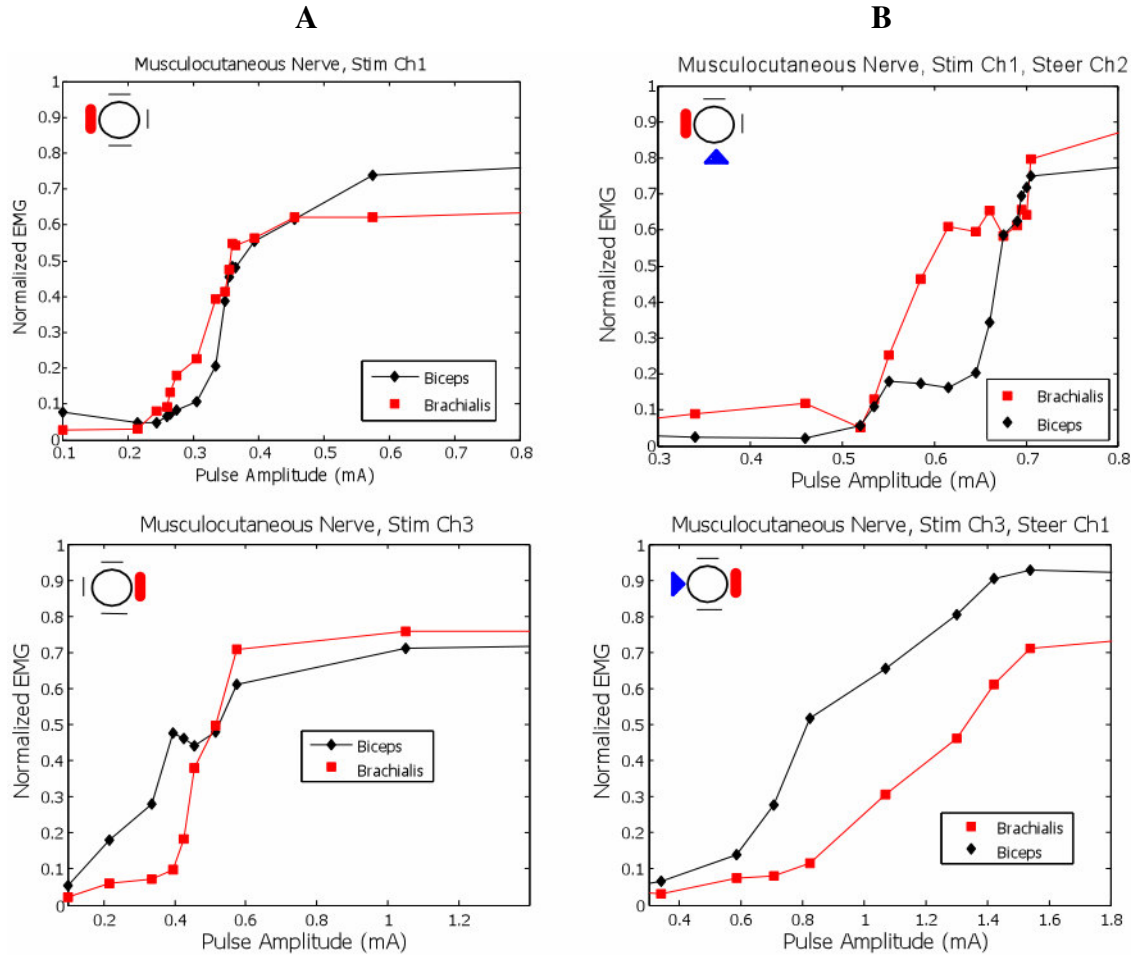


Figure 9. Pulse amplitude modulation recruitment curves from stimulating contact 1 and 3 on the musculocutaneous nerve with a pulse width of 50 μ s. The schematic in the upper left hand corner of each plot visually depicts the channel used for stimulation, thick bar = cathodic stimulation, triangle = anodic stimulation.. (A) Cathodic stimulation of channel 1 results in simultaneous stimulation of the biceps and brachialis. With current steering on channel 2, 70% of brachialis is activated before biceps reaches 20% activation. (B) Cathodic stimulation of channel 3 results in simultaneous stimulation of the biceps and brachialis. With current steering on channel 1, 70% of biceps is activated before brachialis reaches 30% activation..

Moment Production: Moment measurements were made at 7 and 9 weeks post implant to address the effects of exercise and verify that there was no loss of strength. A loss of strength would indirectly indicate a decrease in nerve function due to the implanted electrodes. Measurements were made at four pulse width values. The maximum moments recorded at each session are shown in figures 10 and 11. All electrode contacts produced greater or equal moment about all joints except contact 2 on the musculocutaneous nerve (Figure 10B) and channel 3 on the radial nerve (Figure 11C and 7D) where the fingers switched from a flexion moment to an extension moment. Follow-up shoulder moment from the suprascapular nerve was not measured at week 9 but will be measured at a later date.

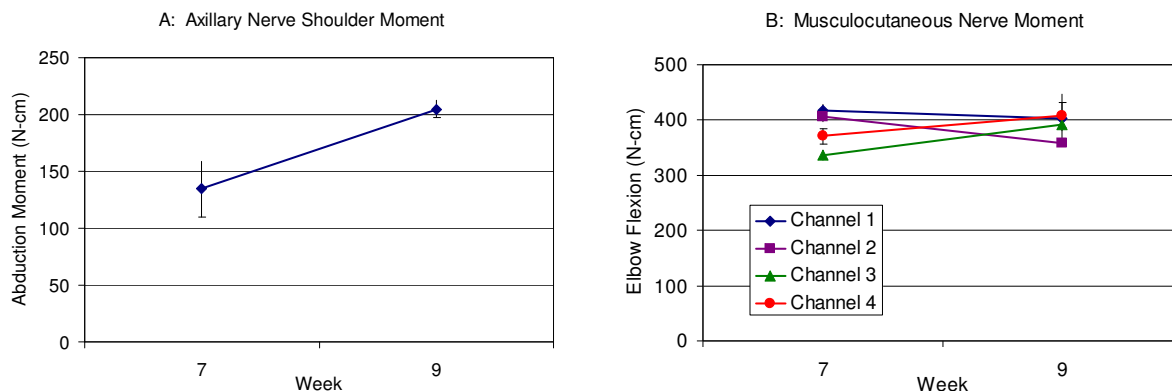


Figure 10. Joint moments measured from axillary and musculocutaneous nerve stimulation at 7 and 9 weeks post implant.

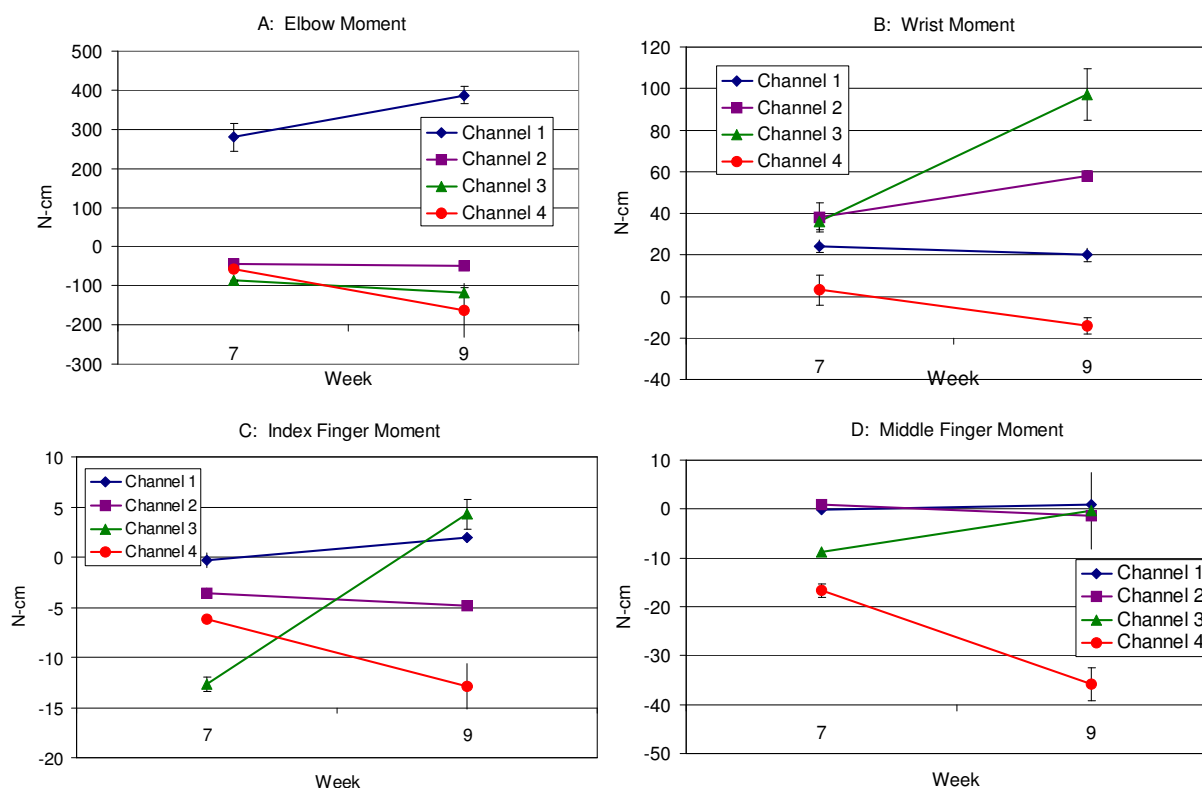


Figure 11. Joint moments measured from radial nerve stimulation at 7 and 9 weeks post implant. Positive Y is an extension moment and negative Y is flexion.

Discussion

The nerve cuff electrodes were placed around entire nerves that contained both motor and sensory fibers. The one subject implanted had an incomplete injury and had full sensation but no motor function (motor C1) on her right arm. Therefore, she was able to feel both the muscles contracting and tactile sensation from stimulation of sensory fibers within the nerve trunk. To date, no specific exploration of her sensation has been performed but it is planned for October.

Current steering was found to increase the selectivity of the cuff electrode on the musculocutaneous nerve. Since the implanted stimulator is monopolar, there are several options for how to stimulate the musculocutaneous nerve without using current steering. Functionally, both the biceps and the brachialis flex the elbow so it is not necessary to distinguish between the two for elbow function. However, the biceps also supinates the forearm. The amount of supination needs to be quantified so that the channel(s) that minimize supination will be attached to the implant. Any unwanted supination that is present if the final system should be able to be balanced by stimulation of the pronator.

Maximally stimulating the axillary and suprascapular nerves together causes abduction of 30-40°. The goal is to achieve 70- 90°. To quantify the force production capabilities of these muscles, the total abduction force was compared to model simulations in the same position. The model predicts that 430 N-cm is required from the deltoid to maintain the arm at 45° of abduction. The measured deltoid abduction was 204 N-cm. However, between 7 and 9 weeks, this abduction moment increases by 50%. Additional increases are expected. The unconstrained abduction should increase with stimulation of the serratus anterior (implant scheduled for November 3). The serratus anterior improves scapular stability as well as rotating the scapula, which should allow for easier abduction.

One unexpected finding from this subject was the activation of finger and wrist flexors from one channel of the radial nerve electrode. These are functions normally produced by the ulnar nerve. The radial and ulnar nerves are not located close together in the arm (where the electrode was implanted) so it unlikely the result of current spillover but there could be some cross over in function in this subject.

Conclusion

This research testing is currently in progress. Weekly experiments will continue until November 3rd when the subject will receive the full upper extremity FES system. The percutaneous connectors will be removed and the electrodes connected to implanted stimulators. The goal is to have the subject controlling her paralyzed arm using voluntary neck EMG signals. The percutaneous phase of this trial has been highly beneficial and demonstrated several key findings.

- Non-penetrating, multicontact cuff electrodes can selectively stimulate individual muscles within a common nerve trunk;
- Selectivity is improved with current steering;
- Intraoperative testing of electrodes is a predictor of chronic performance;
- Nerve stimulation thresholds are an order of magnitude below muscle stimulation;
- Muscle force production is stable or increasing with exercise, indicating no adverse physiological consequences of the electrode implanted on the nerve;

References

K. L. Kilgore, P. H. Peckham, M. W. Keith, F. W. Montague, R. L. Hart, M. M. Gazdik, A. M. Bryden, S. A. Snyder, and T. G. Stage, "Durability of implanted electrodes and leads in an upper-limb neuroprosthesis," *J Rehabil Res Dev*, vol. 40, pp. 457-68, 2003.

Feed-Forward Control of Neuroprosthetic Systems Characterized by Redundant Muscles Acting on Multiple Degrees of Freedom

Contract section:

E.2.a.ii. Simultaneous and natural control of multiple arm and hand functions.

Abstract

We are developing a method of designing feedforward controllers based on inverse models on the musculoskeletal system being controlled. Our two-step design process, based on artificial neural networks (ANN) that are trained with experimentally measured input-output data, provides a unique optimal solution for control. We train two sets of artificial neural networks: the first set as system models, simulating the behavior of the biomechanical model but eliminating the inherent time-variance; the second set as inverse controllers to the musculoskeletal system, predicting stimulation pulsewidths required for achieving desired endpoint-forces.

We are testing the design process in simulation, and we will follow this with experimental tests. For the simulation studies, we created a new static biomechanical model of the thumb and used it to generate time-varying, coupled, and redundant input-output data (i.e., isometric forces at the tip of the thumb in response to electrical stimuli). We created a time-invariant forward neural network model (system model) of the thumb from these data, and used this forward model to average the input-output data, eliminating its time-variance. With the system model, we created optimized input-output data using a minimum co-activation criterion to eliminate redundancy and coupling, obtaining thus a unique solution. We used the optimized and unique input-output data to train an inverse-model static feedforward artificial neural network controller. We tested the controller isometrically in simulation with the biomechanical model of the thumb.

Background

A potentially attractive method for implementing feedforward controllers for musculoskeletal systems with multiple degrees of freedom and complex mechanical interactions is the use of inverse models of the musculoskeletal systems under control. Artificial neural network based controllers offer the advantages of being able to model complex nonlinear relationships using easily obtained input-output data. However, because the relationships between muscle outputs and electrical stimuli are redundant, we need to choose a single inverse solution (i.e., eliminate redundancy) before training the controller.

We previously developed a method for implementing feedforward neuroprosthetic controllers for musculoskeletal systems with multiple degrees of freedom and complex mechanical interactions. These controllers rely on inverse models of the musculoskeletal systems under control. Our tests showed that controller performance was poorer than we expected, and we attributed the poor performance to redundancy of the data used to train the controllers. The inverse relationship between muscle output and electrical stimulation is not unique (most joints have redundant actuation with non-stationary input-output muscle properties and coupled degrees of freedom) and if left unrestricted, the controller implementation process may result in an unsuitable inverse. Thus, we must choose a single inverse solution before the controller is

created. Our present work involves obtaining this unique inverse solution and using it to train a controller capable of providing independent control of coupled degrees of freedom.

Proper training of artificial neural network-based controllers sometimes requires large amounts of data that cannot be collected in a single experimental session. It has been our experience that SCI individuals who have received an implanted neuroprosthesis have busy schedules and/or difficulties visiting the hospital for research participation. This lack of availability limits the amount of data we can obtain and makes controller fine-tuning more difficult. For this reason, we created a model of a human thumb to help us develop and fine-tune the inverse controller. This in turn will allow us to estimate the minimal amount of data we need to collect with the SCI population, hopefully decreasing the time each individual has to spend in the laboratory.

Our general approach was to first create a time-invariant forward neural network model (system model) of a computer-simulated thumb using time-varying, coupled and redundant data relating muscle stimuli to muscle outputs. We used the forward model to average the input-output data and thus eliminate its time-variance. We then chose unique input-output data from the time-invariant set to optimize specific performance criteria, such as minimum co-activation, allowing us to eliminate redundancy and thus obtaining a unique solution. We trained an inverse-model, static, feedforward, artificial neural network controller with these optimal input-output data. We tested the controller isometrically with the simulation model.

Structure of the biomechanical model

Skeletal model

We created, in simulation, a static biomechanical model of a human thumb that allows us to generate time-varying, coupled, and redundant input-output data (i.e., isometric forces at the tip of the thumb in response to electrical stimuli).

We modeled the thumb as two cylindrical rigid bodies (the metacarpal bone and phalanges) connected by a revolute (metacarpophalangeal, MP) joint. We modeled the proximal and distal phalanges as a single rigid body by fixing the interphalangeal (IP) joint when the longitudinal axes of the proximal and distal phalanges were colinear. The proximal end of the metacarpal bone was attached to a universal (carpometacarpal, CMC) joint linking it to the trapezium, which was fixed in space (i.e., no arm rotation was allowed). The tip of the thumb was also fixed in space to a force/moment sensor so we could measure isometric forces (Figure 12). The geometric parameters were taken from the literature, and are summarized in Table 1.

Table 1. Skeletal parameters of the thumb [Esteki 1995, Esteki and Mansour 1997].

Bone	Length (cm) ¹	Radius (cm) ¹	Specific mass (g/cm ³) ²
Metacarpal	7.20	1.50	1.1
Proximal phalanx	3.90	1.10	1.1
Distal phalanx	2.00	1.10	1.1

¹ Esteki 1995, ² Esteki and Mansour 1997.

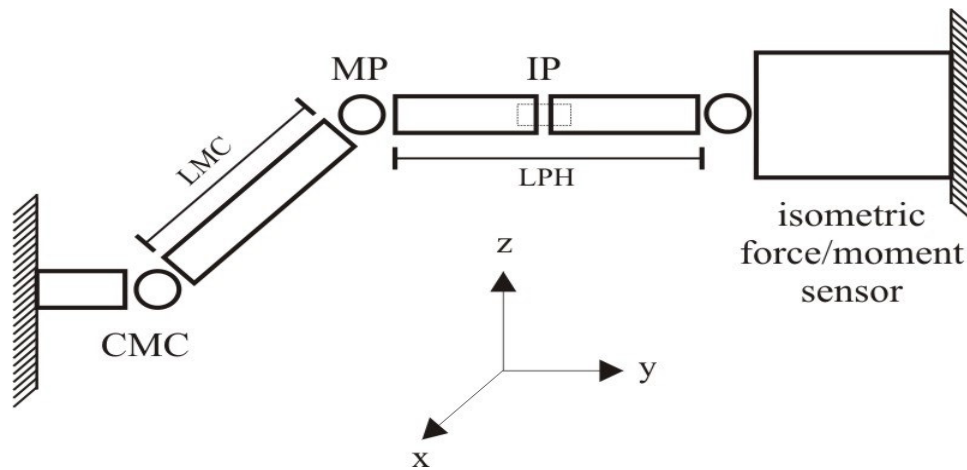


Figure 12. The trapezium and the tip of the thumb are both fixed in space. The IP joint is fixed. The MP joint is modeled as a revolute joint while the CMC joint is modeled as a universal joint. The Cartesian coordinate system is fixed.

We control the isometric forces at the tip of the thumb through moments acting at the CMC and MP joints. The two degrees of freedom (i.e., flexion/extension and abduction/adduction) are actuated by four muscles (extensor pollicis longus (EPL), abductor pollicis brevis (AbPB), adductor pollicis (AdP), and flexor pollicis longus (FPL)). Since the muscles have moment arms about both axes, their actions are coupled, and since there are more muscles than degrees of freedom, there is redundancy.

Muscle model

Individual muscle forces will depend primarily upon their muscle activations and time (i.e., the geometry of the muscle and nerve with respect to the stimulating electrode will not change significantly).

The peak isometric force and muscle geometric parameters for the four muscles included in the model were taken from the literature [Esteki and Mansour 1997, Brand et al. 1981] or estimated using parameters taken from the literature, and are summarized in Table 2.

Table 2. Muscle parameters. L_o represents the optimal muscle length. F_o is the maximum force produced when the muscle is at its optimal length. L_{st} is the tendon slack length.

Muscle	L_o (cm) ^{2,3}	F_o (N) ²	L_{st} (cm) ⁴
EPL	5.7	38	21
FPL	5.9	102	32.15
AdPo	3.6	18	2.25
AdPt	3.6	48	3.5
AbPB	3.7	30	2.55

² Esteki and Mansour 1997, ³ Brand et al. 1981, ⁴ Estimated.

For simplicity, we used a Hill based muscle model incorporating only length-tension properties. We omitted activation dynamics and force-velocity properties because we will perform static analysis only. We modeled muscle force (F_m) with the equations given below.

Where

$$\tilde{F}_m = f(i)AF_o [L\tilde{T}(\tilde{L}_m)]$$

$$L\tilde{T}(\tilde{L}_m) = -3.05\tilde{L}_m^2 + 5.98\tilde{L}_m - 1.96$$

$$\tilde{L}_m = L_m / L_o$$

$$L_m = L_{mt} - L_t$$

$$L_{mt} = L' + \int_0^{\theta_2} r(\theta_2) d\theta_2 + \int_0^{\theta_1} r(\theta_1) d\theta_1 + \int_0^{\phi_1} r(\phi_1) d\phi_1$$

$$L_t = L_{st} + \frac{F_m}{K_T}$$

$$K_T = \frac{F_o}{0.0325L_{st}}$$

F_m	= muscle force
$f(i)$	= fatigue factor
A	= muscle activation
K_T	= tendon stiffness
r	= moment arm
θ_2	= MP flexion/extension angle
θ_1	= CMC flexion/extension angle
ϕ_1	= CMC abduction/adduction angle
L_m	= muscle length
L_t	= tendon length
L_{mt}	= muscle-tendon length
L_{st}	= tendon slack length
L'	= muscle-tendon unit length when all joints are at 0°
L_o	= optimal muscle fiber length
\sim	= normalized

Muscle activation was modeled as a nonlinear function of the electrical stimulus u given by a sigmoidal relationship of the form $A(u) = \frac{1}{(1 + e^{-u})}$ (Figure 13).

To account for the time-varying properties of muscle, we introduced the linearly-decreasing normalized fatigue factor $f(i)$ (Figure 14) to scale the maximum muscle force F_o . The fatigue factor reduced the maximum muscle force by 4.2% per 100 muscle contractions [Kilgore 1987]. We also added or subtracted random noise (as 10% of the muscle force) to the muscle force with every muscle contraction. We assume muscle potentiation is eliminated by conditioning contractions prior to performing any measurements.

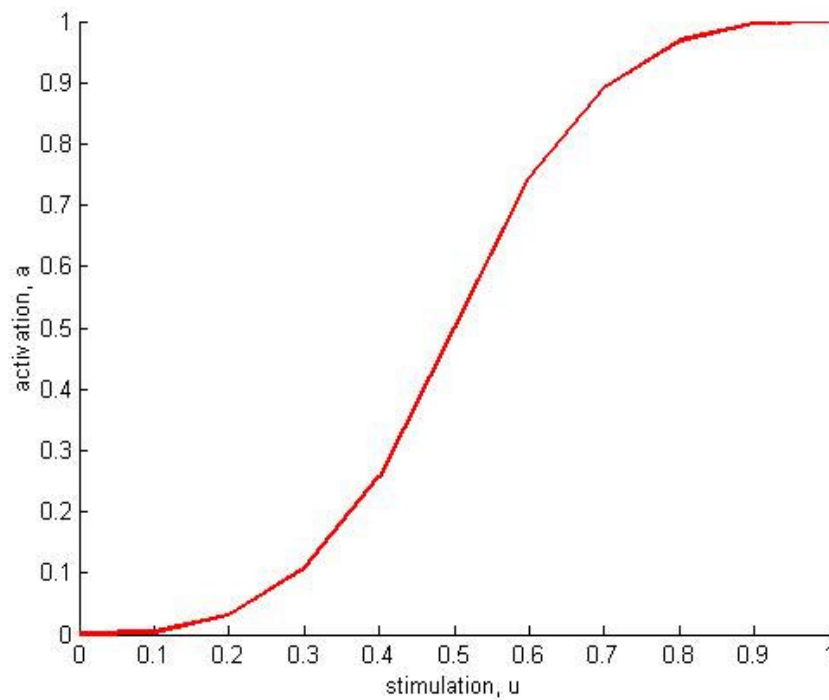


Figure 13. Simple nonlinear recruitment characteristics. Muscle activation as a function of normalized muscle stimulus.

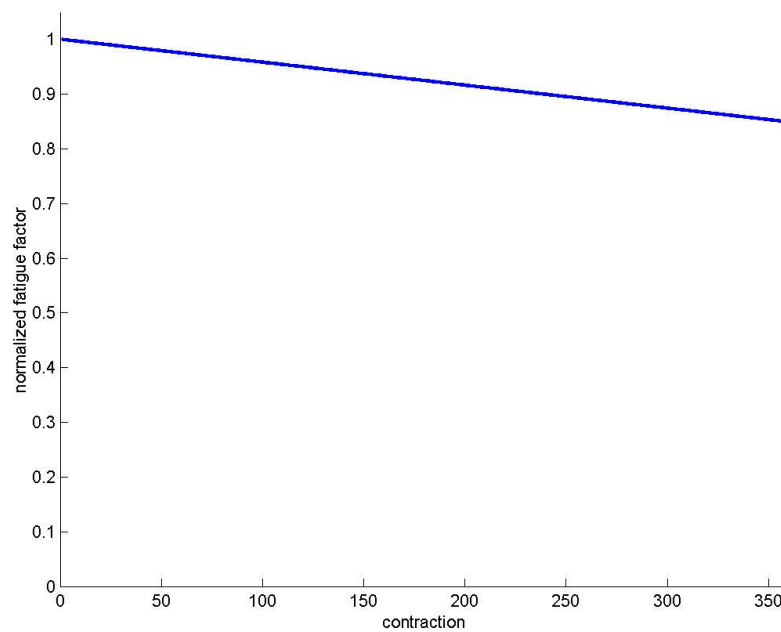


Figure 14. Normalized fatigue factor $f(i)$ as a function of muscle contraction.

Model equations

The thumb model, which we will refer to as the limb model, is defined by the equation $\tau = J^T F$. Thus, to find the end-point forces, we solve for $F = (J^T)^{-1} \tau$, where

$$\tau = \begin{bmatrix} M_{CMC_AA} \\ M_{CMC_FE} \\ M_{MP_FE} \end{bmatrix}$$

$$J^T = \begin{bmatrix} LTIP & 0 & 0 \\ 0 & -LMC \sin(\theta_1) - LPH \sin(\theta_1 + \theta_2) & LMC \cos(\theta_1) + LPH \cos(\theta_1 + \theta_2) \\ 0 & -LPH \sin(\theta_1 + \theta_2) & LPH \cos(\theta_1 + \theta_2) \end{bmatrix}$$

$$F = \begin{bmatrix} F_x \\ F_y \\ F_z \end{bmatrix}$$

$$M_{CMC_FE} = \sum_i r_i(\theta_1) \cdot Fm_i$$

$$M_{MP_FE} = \sum_i r_i(\theta_2) \cdot Fm_i$$

$$M_{CMC_AA} = \sum_i r_i(\phi_1) \cdot Fm_i$$

$$LTIP = LPH \cos(\theta_1 + \theta_2) + LMC \cos(\theta_1)$$

and

- F_x = Force exerted at the tip of the thumb along x axis.
- F_y = Force exerted at the tip of the thumb along y axis.
- F_z = Force exerted at the tip of the thumb along z axis.
- LPH = Phalanges length.
- LMC = Metacarpal length.
- $LTIP$ = Distance from the base of the metacarpal to the tip of the phalanges on the y-z plane.
- M_{MP_FE} = Flexion/extension muscle moment exerted at the MP joint.
- M_{CMC_FE} = Flexion/extension muscle moment exerted at the CMC joint.

M_{CMC_AA} = Abduction/adduction muscle moment exerted at the CMC joint.

J^T = Transpose of the Jacobian matrix.

θ_1 = Metacarpal flexion/extension angle.

θ_2 = Phalanges flexion/extension angle.

ϕ_1 = Metacarpal abduction/adduction angle.

R = Moment arm as a function of angle.

i = Each muscle.

Computer Simulations

Data collection

We fixed the CMC joint at 20 degrees of extension ($\theta_1=20$) and 15 degrees of adduction ($\phi_1=15$), and the MP joint at 20 degrees of flexion ($\theta_2=-20$) (Figure 15).

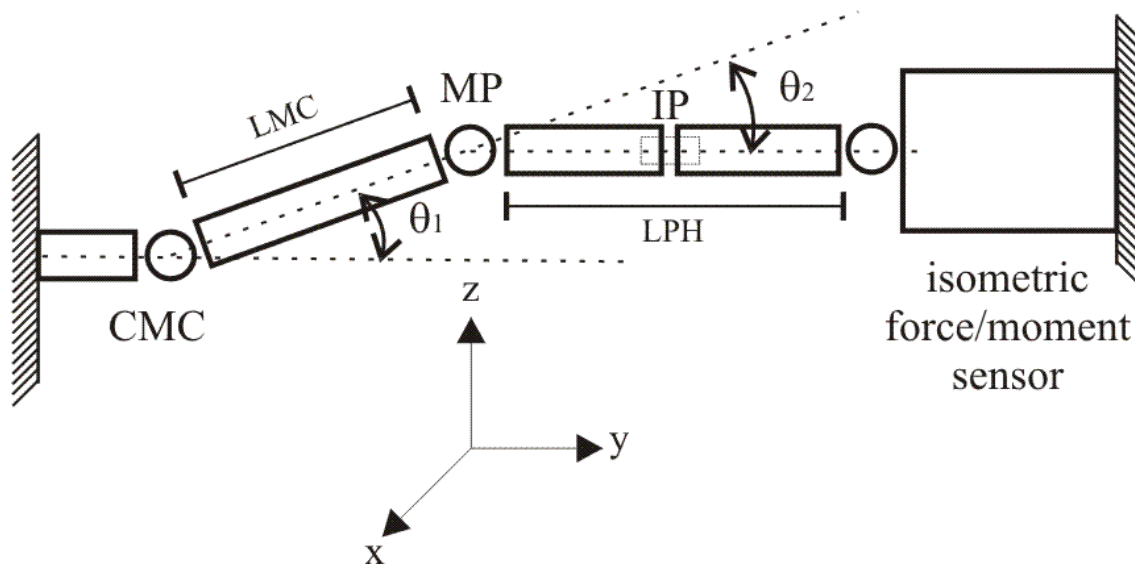


Figure 15. Thumb model in the y-z plane. The coordinate system is expressed with respect to the CMC joint. The y-z plane is rotated about the z-axis with changes in ϕ_1 . $\theta_1=20$ (extension), $\phi_1=15$ (adduction), and $\theta_2=-20$ (flexion).

The simulations were performed with 10% random noise in each muscle (i.e., with independent noise distributions) and a fatigue rate of 4.2% per 100 muscle contractions.

We generated time-varying coupled and redundant input-output data with the limb model by controlling the muscle forces with stimulus pulsewidths. We used the origin (i.e., no stimulation) in addition to another six pulsewidths that result in seven equally-spaced activations spanning the activation range (Figure 16), ensuring we covered the space of possible input-

output combinations. We stimulated all muscles simultaneously at all combinations of pulsewidths for a total of 7^3 (343) trials (Figure 17, bottom) and measured the contact forces at the thumb tip in the x-z plane for each pulsewidth combination, (Figure 17, top).

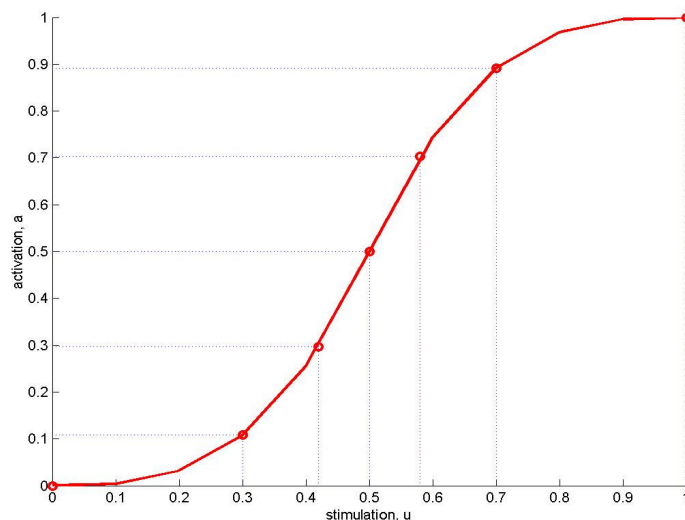


Figure 16. Initial pulsewidths spanning the muscle activation range.

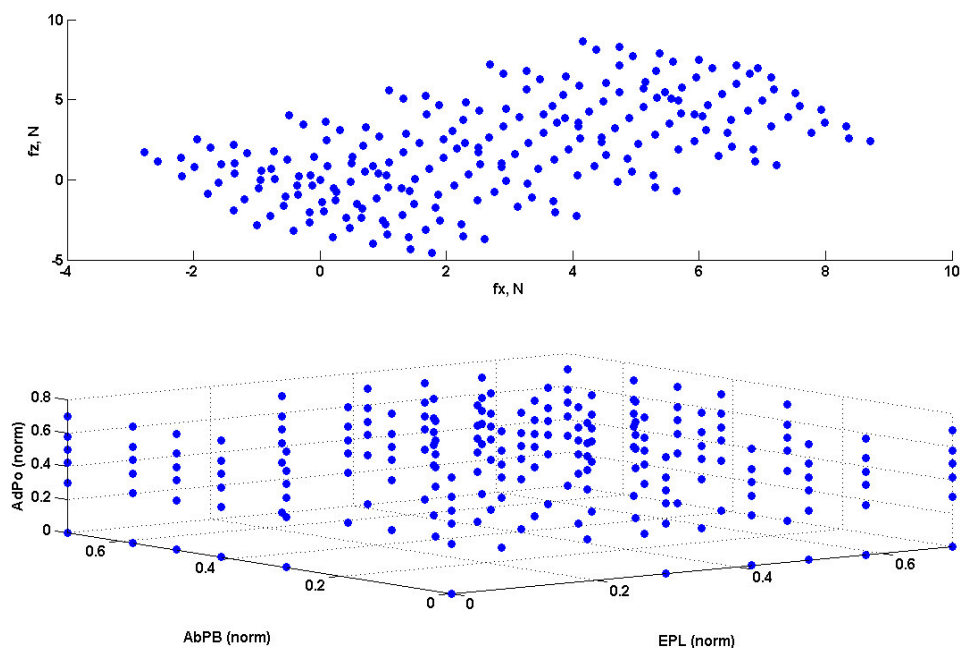


Figure 17. Forces measured in the x-z plane during stimulation of three muscles: extensor pollicis longus (EPL), abductor pollicis brevis (AbPB), and adductor pollicis (ADP). For clarity, only 216 points are shown.

System Model

We used these data to implement a deterministic neural network system model. This system model is a time-invariant forward model of the biomechanical model. The neural network has three inputs (EPL, AbPB, and AdP pulsewidths), six hidden neurons, and two outputs (Fx, and Fz). The neural network also has sigmoidal [Narendra and Parthasarathy 1991] and linear [Jonic et al. 1999] transfer functions for the hidden and output layers respectively.

We trained the system model off-line on a data subset containing 80% of the time-varying input-output data measured. The other twenty percent of the data was randomly removed and used as a validation set to prevent data over-fitting (i.e., the validation set was used to stop training if further training would result in worse generalization). We selected the Levenberg-Marquardt algorithm because we have a small network size, small amounts of data, and used off-line training [Demuth and Beale 2000, Reed and Marks 1999, Jonic et al. 1999]. The training has a variable learning rate with a random initial selection of the weights.

We trained the system model for 1000 epochs. Training was stopped ahead of time if the validation mean squared error (MSE) increased or if the fitting MSE goal ($1e-6$) was reached. Preliminary results suggested that training neural networks like the one described above for more than 1000 epochs do not result in improved generalization capabilities and may result in data overfitting. Furthermore, when the validation set is used, training is always terminated before 600 epochs.

No amount of training can create information that is not contained in the training data. Thus, by using pulsewidths that result in equally-spaced activations spanning the activation range (Figure 16) and taking advantage of the good interpolating capabilities of artificial neural networks, we can ensure that the network generates accurate force predictions even for inputs not included in the training data set.

Network generalization also depends on the initial weights, so we trained 10 neural networks using different random initial weights and selected the network with the smallest fitting MSE (i.e., when presented with the training data) as our system model.

Unique solution

We used the trained system model to generate smooth time-invariant data (Figure 18). We input pulsewidths ranging from activation threshold to saturation to the system model and generated the corresponding outputs, generating more data than previously measured from the static biomechanical model.

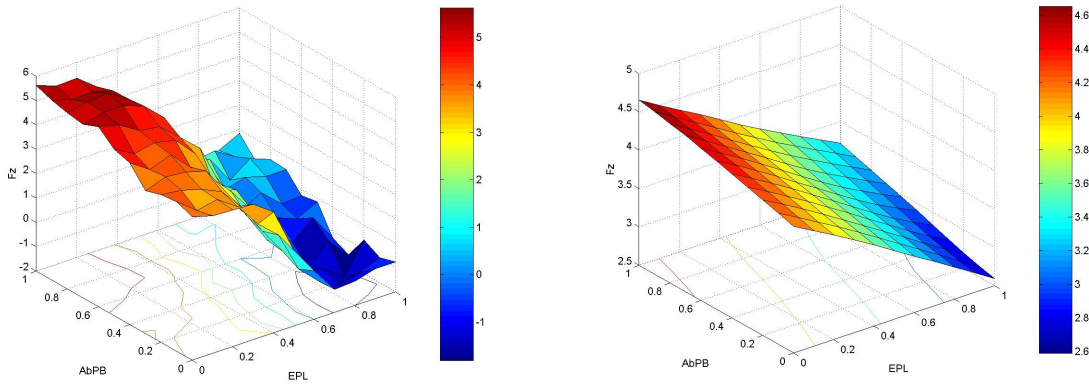


Figure 18. System model eliminates time variance. e.g., F_z as a function of muscle stimulation. AdPo is held at constant stimulation ($U_{ADP}=0.5$). Solutions are represented as contours characterizing the redundant input-output properties of the model for different levels of muscle activation.

The data generated with the system model contains redundancies due to muscle cocontraction. We defined a cocontraction cost function that measures the goodness of each solution by calculating its energy. We defined energy (E) as the sum of the squares of the normalized muscle activations $E = (U_{EPL}^2 + U_{APB}^2 + U_{ADPo}^2)$.

Our optimization criterion for eliminating redundancy from the system model input-output data by minimizing the total normalized muscle activation was the following:

$$\text{minimize } [E = (U_{EPL}^2 + U_{APB}^2 + U_{ADPo}^2)] \text{ such that } (\hat{F}_x - F_x)^2 + (\hat{F}_z - F_z)^2 = 0, \text{ where}$$

E = Energy

U = Stimulus pulsewidth applied to each muscle

F_x = Force exerted at the tip of the thumb along x axis

F_z = Force exerted at the tip of the thumb along z axis

\hat{F}_x = Desired force at the tip of the thumb along x axis

\hat{F}_z = Desired force at the tip of the thumb along z axis

Reduction in muscle cocontraction decreases muscle fatigue, so it is important to determine if the optimization process resulted in decreased activations. To do this we selected a set of target force vectors across a subset of the force domain (Figure 19) and compared the pulsewidths necessary to achieve those target forces predicted by a controller trained on optimized data and a controller trained on non-optimized data. The polar plots in Figure 20 show that the optimization process resulted in decreased activations for all three muscles in most force directions (Figure 20a), and that there was a general reduction of energy with respect to the non-optimized controller (Figure 20b).

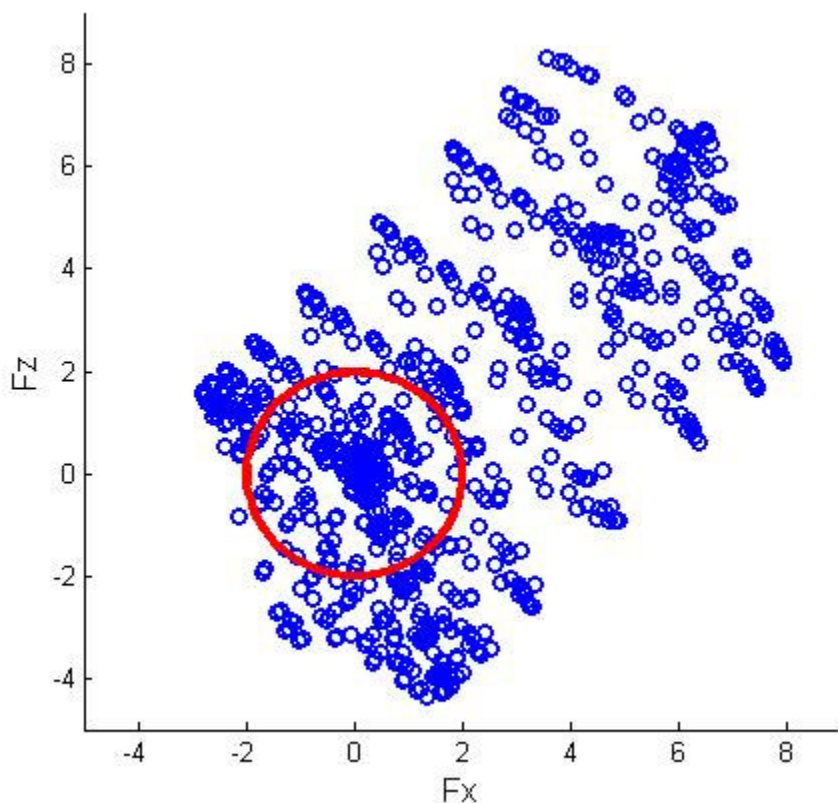


Figure 19. The area spanned by the blue dots represents the domain of possible forces. The red circle represents the target force vectors with a magnitude of 2N around the origin used to test the trained inverse controllers and compare the energies between optimized and non-optimized controllers.

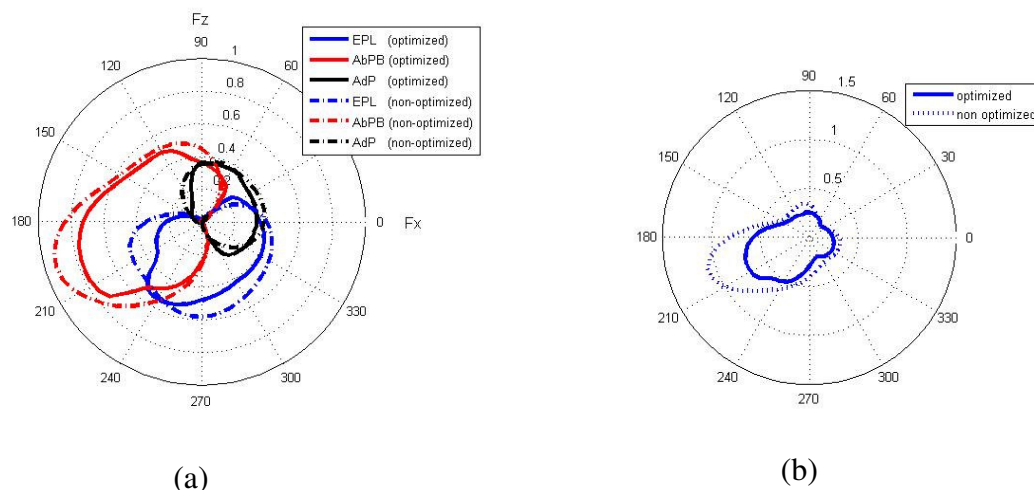


Figure 20. Pulsewidths and energies produced by the optimized and non-optimized controllers in response to the target forces (i.e., circle) shown in Figure 19 as a function of force vector angle. (a) The optimized pulsewidths are lower than the non-optimized in most force directions. (b) The energy for the optimized controller pulsewidths is always lower than the non-optimized controller energy.

We performed a partial monotonicity test of the system model by systematically fixing two inputs (i.e., stimulus pulsewidths to two muscles are set to zero) and monotonically modulating the other, verifying that the force output (i.e., along both axes) also varies monotonically and therefore guaranteeing the uniqueness of the data (Figure 21). To fully test for monotonicity we would need to apply this criterion to all possible combinations of stimulus pulsewidths for all three muscles.

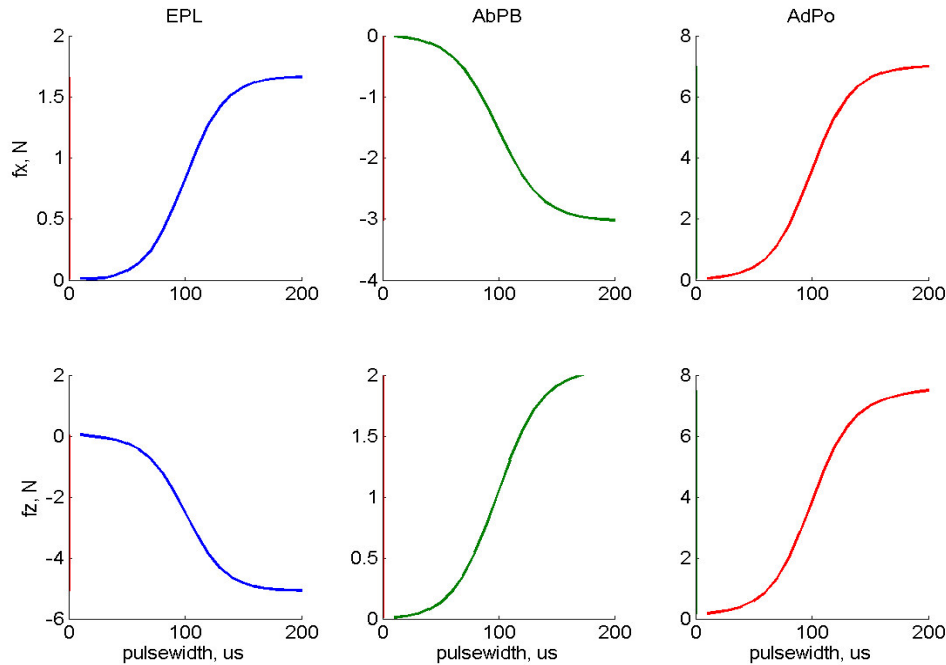


Figure 21. Forces measured in the x and z axes during stimulation of only one muscle in the system model while the other two are not stimulated. (e.g., when the extensor pollicis longus (EPL) is stimulated, abductor pollicis brevis (AbPB) and adductor pollicis (ADP) are not).

Inverse Controller

We trained a second ANN as a deterministic inverse model of the thumb using the optimal input-output data. The architecture of the feedforward controller was similar to that of the system model: sigmoidal and linear transfer functions for the hidden and output layers respectively, with two inputs (forces along x and z axes), six hidden neurons, and three outputs (stimulus pulsewidths for all three muscles). We trained the feedforward controller using the Levenberg-Marquardt algorithm for the same conditions as the system model (i.e., measuring MSE with an error goal of $1e-6$ and training for up to 1000 epochs). We trained 10 neural network controllers using different random initial weights and selected the network with the smallest fitting MSE as our inverse controller.

Controller Test

We tested the ability of the feedforward inverse controller to predict stimulus pulsewidths required for control of the limb model under isometric conditions. First we specified different

sets of target forces in the x and z directions (e.g., two different force magnitudes about two axes: flexion/extension and adduction/abduction) within the training data domain and then used the feedforward controller to predict the stimulus pulsewidths required to elicit these target outputs. We then stimulated the limb model with these pulsewidths and measured the actual outputs of the limb model in response to stimulation. Note that the limb model included noise and fatigue, which are at least partially responsible for the variable error.

Figure 22 shows two sets of target forces over two different areas of the force domain with their respective actual forces resulting from limb model stimulation using pulsewidths predicted by optimized and non-optimized inverse controllers.

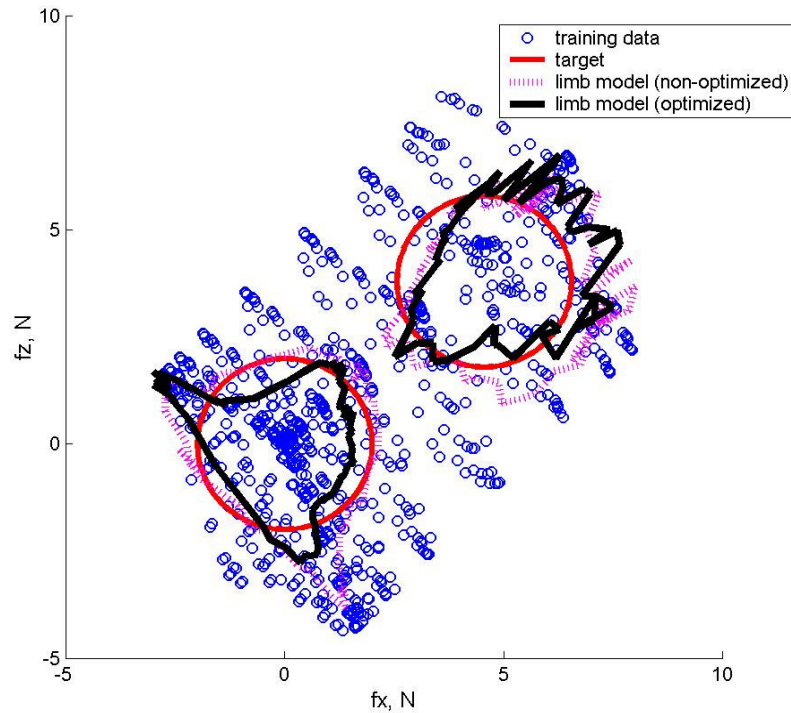


Figure 22. Target and actual forces in response to controller-predicted stimulation over two regions of the force domain. The pulsewidths are not shown. The black and magenta lines are the actual forces generated by the limb model when stimulated with the pulsewidths predicted by the optimized and non-optimized inverse controllers, respectively, in response to the target forces shown by the red circles.

Figure 23 shows a third set of target forces with the respective actual forces resulting from stimulation with controller-predicted pulsewidths over an evenly-sampled area of the force domain. The errors between the target and actual forces are small. The pulsewidths predicted by the optimized inverse controller are shown. Optimization guarantees that not all muscles are stimulated at high levels at the same time reducing muscle cocontraction.

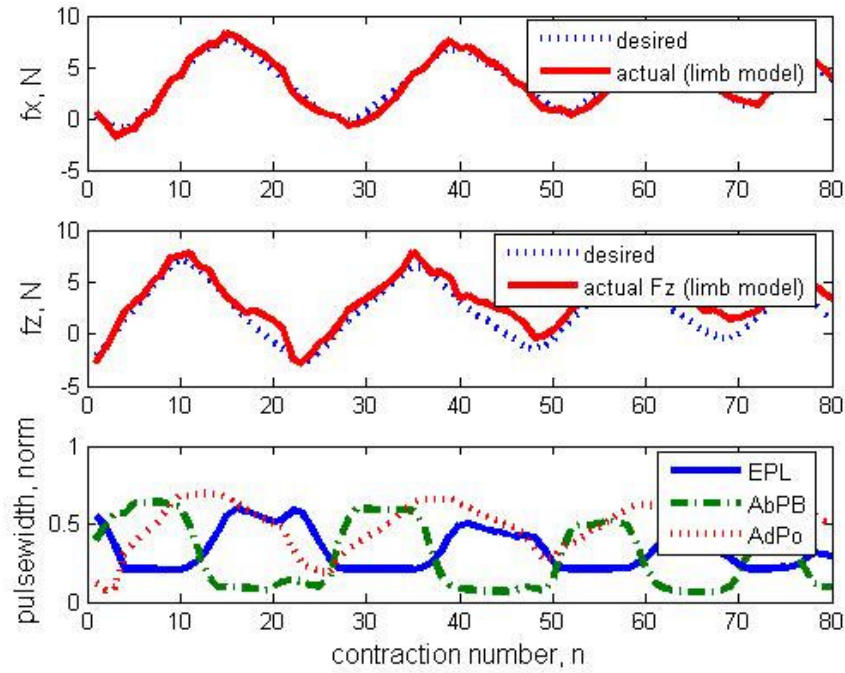


Figure 23. Upper plot: Dotted line shows the desired (i.e., target) forces while the solid line shows the actual forces, along the x axis. Middle plot: Target and actual forces along z axis. Bottom plot: Activation pulsewidths predicted by the optimized inverse controller. Not all muscles are stimulated at high levels at the same time.

The optimized inverse controller resulted in good force tracking throughout the force domain for the tests depicted in Figures 22 and 23 in the presence of noise and muscle fatigue.

Performance Analysis

We performed a statistical comparison between the target and actual limb model outputs to determine the effectiveness of the controller. An effective controller is one for which the differences between the actual and target forces are small (i.e., root mean squared error less than 2N) and mainly due to variability in the limb model and not induced by the controller. We analyzed controller performance with two variability measurements: system variability and total variability.

The system variability indicates how much the limb model outputs vary with time (e.g., variability due to noise and muscle fatigue). We estimated system variability by comparing two sets of limb model outputs ($F_{actual1}$ and $F_{actual2}$) generated at two different times in response to the same inputs (i.e., pulsewidths predicted by the controller in response to F_{target}).

$$S_s^2 = \text{system_variability} = \frac{\sum_{i=1}^k (F_{actual1}(x_i) - F_{actual2}(x_i))^2}{k},$$

where x_i is the pulsewidth vector at iteration i , and k is the number of input/output combinations in the data set.

Total variability is a measurement of the difference between the targets and the actual limb model outputs and provides an indication of the suitability of the network-predicted pulsewidths for achieving the targets (i.e., prediction error).

$$S_T^2 = \text{total_variability} = \frac{\sum_{i=1}^k (F_{\text{target}_i} - F_{\text{actual}_i}(x_i))^2}{k}$$

If the square root of the system variability was higher than 30% of the mean limb model output (i.e., $S_s > 0.3\bar{F}_{\text{target}}$) we considered the limb model as not controllable and therefore we could not evaluate controller performance. If the system was controllable (i.e., $S_s \leq 0.3\bar{F}_{\text{target}}$), we evaluated controller performance by first comparing the total variability to the system variability. For the tests performed, the square root of the system variability was between 0.6 and 0.7N while the mean limb model output was 1.1N.

We tested an equality of variances hypothesis $H_o : S_s^2 = S_T^2$ using a Modified Levene Test ($F_o = S_s^2 / S_T^2$). The rejection criteria were $F_o > F_{\alpha/2, n_1-1, n_2-1}$ or $F_o < F_{1-(\alpha/2), n_1-1, n_2-1}$, where $F_{\alpha/2, n_1-1, n_2-1}$ and $F_{1-(\alpha/2), n_1-1, n_2-1}$ represented the upper .025 and lower 0.975 percentage points of an F distribution with n_1-1 and n_2-1 degrees of freedom ($\alpha=0.05$).

We failed to reject the null hypothesis (H_o) with p-values > 0.2 . We tested a second hypothesis of equality of means $H_o' : \mu_{\text{target}} = \mu_{\text{actual}}$ using a t-test. We also failed to reject the null hypothesis (H_o') with p-values > 0.7 . This evidence suggested that the controller was not adding significant variability to the force errors.

Conclusions

The results suggested that it is possible to design an inverse controller from input-output data and that the controller accurately predicts the pulsewidths required to achieve the desired outputs. We also showed that we can use a system model to eliminate time-variance from the data and an optimization process to eliminate redundancy.

Next Quarter

We will perform a series of computer simulations to determine the optimal number of hidden neurons for the system model and inverse controller. We will systematically vary the number of hidden neurons in the system model and inverse controller and measure the force prediction error and energy used.

We will test the controller isometrically with able-bodied and spinal cord injured human subjects. We will first study redundancy by stimulating only a pair of antagonists (extensor pollicis longus and abductor pollicis brevis) controlling flexion/extension of the thumb's carpometacarpal joint. We will incorporate coupling to the system by stimulating an additional muscle (adductor pollicis) allowing us to control abduction/adduction as well. We will use the same approach used in the computer simulations for the real musculoskeletal systems studies.

We have obtained IRB approval for surface stimulation and are in the progress of obtaining a surface stimulator that can be controlled in real-time with a computer.

References

- Brand P.W., Beach R.B., Thompson D.E. (1981) "Relative tension and potential excursion of muscles in the forearm and hand", *J. Hand Surgery [Am]*, Vol. 6 (3), May, 209-219.
- Demuth H., Beale M. (2000) "Neural Network Toolbox. User's guide" The MathWorks.
- Esteki A. (1995) "Dynamic model of the hand with application in functional neuromuscular stimulation", Ph.D. Dissertation, Case Western Reserve University.
- Esteki A., Mansour J.M. (1997) "A dynamic model of the hand with application in functional neuromuscular stimulation", *Annals of Biomedical Engineering*, Vol. 25, No 5.
- Jacobson M.D., Raab R., Fazeli B.M., Abrams R.A., Botte M.J., Lieber R.L. (1992) "Architectural design of the human intrinsic hand muscles", *J. Hand Surgery [Am]*, Vol. 17A (5), Sept, 804-809.
- Jonic S., Jankovic T., Gajic V., Popovic D. (March 1999) "Three machine learning techniques for automatic determination of rules to control locomotion", *IEEE Trans. On Biomedical Engineering*, Vol. 46, No. 3, 300-310.
- Kilgore K.L. (1987) "Force vector recruitment of electrically stimulated paralyzed thenar muscles with application to functional neuromuscular stimulation", M.S. Thesis, Case Western Reserve University.
- Kirsch RF. et al, "Restoration of Hand and Arm Function by Functional Neuromuscular Stimulation", Quarterly Progress Report #5, NIH Neuroprosthesis Contract N01-NS-1-2333, 21-27, June 2002.
- Lewis S. (2001) "Metacarpophalangeal pattern profile analysis of a sample drawn from a North Wales population", *Annals of Human Biology*, Vol. 28 (5), 589-593.
- Lieber R.L., Jacobson M.D., Fazeli B.M., Abrams R.A., Botte M.J. (1992) "Architecture of selected muscles of arm and forearm: anatomy and implications for tendon transfer.", *J. Hand Surgery [Am]*, Vol. 17A (5), Sept, 787-799.
- Lujan J.L., Crago P.E. (2004) "Computer-based test-bed for clinical assessment of hand/wrist feed-forward neuroprosthetic controllers using artificial neural networks", *Med Biol Eng Comput.*, 42(6), Nov, 754-61.
- Narendra K.S., Parthasarathy K. (March 1991) "Gradient methods for the optimization of dynamical systems containing neural networks", *IEEE Transactions on Neural Networks*, Vol. 2, No. 2, 252-262
- Reed R.D., Marks R.J. (1999) "Neural Smithing. Supervised learning in feedforward artificial neural networks", MIT Press, Cambridge, MA..

Secco E.L., Magenes G. (2002) "A life-like control algorithm for the natural movement of a 3 DOF finger", *Proceedings of the Second Joint EMBS/BMES Conference*, Houston, TX. USA. October 23-26.

Valero-Cuevas F.J., Johanson M.E., Towles J.D. (2003) "Towards a realistic biomechanical model of the thumb: the choice of kinematic description may be more critical than the solution method or the variability/uncertainty of musculoskeletal parameters", *Journal of Biomechanics*, Vol. 36, 1019–1030

Real-time EEG control of virtual cursor/arm movements

Contract section: E.1.a.iv Command sources for high tetraplegia

We found some bugs in our earlier software for adaptively decoding EEGs into multidimensional cursor movements. This revised software now works even better than before and has enabled two subjects to very rapidly achieve significant 2D cursor control within the first training session via the same adaptive decoding process previously used in monkeys (Taylor et al, 2002). (Note one subject had no prior training and the other had one 30-minute training session 3 months earlier which was unlikely to have any impact on initial performance after that long of a delay). In our previous monkey studies, the coadaptive algorithm was used with intracortical firing rates. In this study the same algorithm is used only the inputs are the power in different frequency bands at different electrode locations. This rapid learning of 2D control from scalp surface EEGs is unprecedented as previous reports in the literature suggest many weeks of training is necessary for 2D control from the low resolution scalp surface EEG (Wolpaw, et al 2004). Figure 24 shows EEG controlled trajectories from one subject after only 40 minutes of training in a 1D task followed by 20 minutes of training in the 2D task. Although this is far from perfect, trajectories to the four targets (differentiated by color) clearly tend to go in distinctly different directions over the 2D workspace.

The linear decoding we used showed consistent errors, including a tendency to move more in diagonal directions than horizontal or vertical direction. This problem is characteristic of a positive correlation between the features of the signals that are being used for horizontal and vertical control. We then created a transformation function that specifically normalizes for these

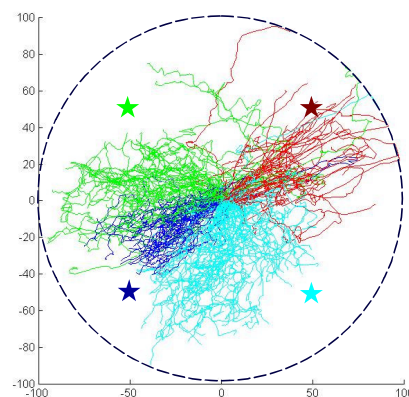


Figure 24. 2D trajectories generated by willful modulation of scalp surface EEGs after subject had only 20 minutes of coadaptive training in this 2D task. Random weights were used in the initial decoder and were iteratively adjusted every few minutes based on the neural activity seen during attempted movements. Trajectories are color coded by intended target. Actual target positions are shown by the four stars.

sorts of correlations in the neural data (i.e. correlations that result in oval trajectory distributions along a diagonal). Figure 25 illustrates this simplistic normalization function.

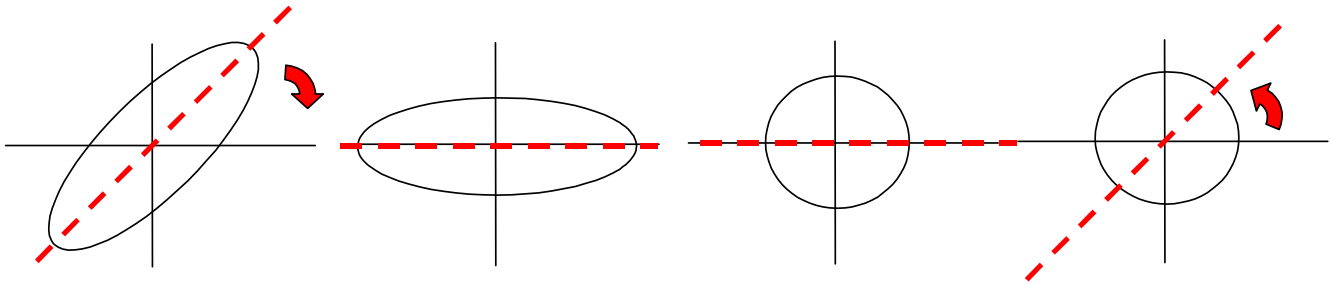


Figure 25. Simple correlation correction procedure. At each time step, the velocity vector is rotated 45 degrees, normalized to the same average magnitude in the vertical and horizontal direction (e.g. $x' = x * E[x+y/2]/E[x]$ where $E[]$ indicates 'expected value' determined from an initial set of data gathered before compensation), and then rotated back 45 degrees to the original orientation.

Figure 26 shows trajectories that were made by including this simple correlation compensation procedure at each timestep in a center out 2D real-time cursor control task. Although this correlation correction procedure did more evenly distribute trajectories throughout the workspace, there were still asymmetries that were not corrected via this simple correlation correction algorithm

We are now working on a simple neural network based non-linear transformations of the decoder outputs to achieve a more uniform level of control throughout the workspace. Decoder output non-linearities were something often seen in our prior monkey work where multichannel unit activity was decoded using linear decoding algorithms. Although the animals eventually learned to modify their neural activity to better match the imposed linear decoding function, developing methodologies for including an efficient non-linear transformation step at the *output* stage of the decoder can have applications that go beyond the EEG-based cursor control shown here. These methodologies can be applied to any biopotential signals (intracortical unit activity, ECoG, EMGS, etc). Inherently, using a linear mapping of high dimensional 'neural space' (e.g. many electrode channels) to a low dimensional output space (limb endpoint and hand orientation control) is most efficient. Then a non-linear transformation can be more efficiently applied in the low-dimensional output space to correct for the fact that the inputs were actually non-linear in nature.

Combined EEG/EMG control from the same electrodes.

Scalp surface or subcutaneous EEG signals gathered over the motor areas of the brain are inevitably going to be contaminated with EMG artifacts from jaw activity. These EMG artifacts

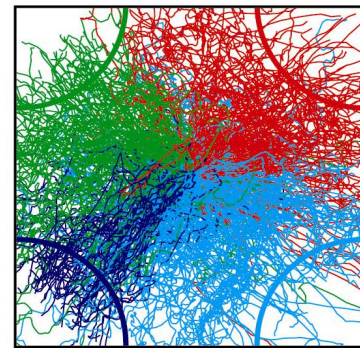


Figure 26. EEG-controlled trajectories made via the linear adaptive decoding algorithm followed by a simple real-time correlation compensation procedure at each timestep. Trajectories are color coded by intended target.

in the EEG signal can be looked at as a problem or as an opportunity. They are problematic in that naturally occurring EMGs from swallowing, chewing, talking, etc. can interfere with the normal EEG signal, and periodic swallowing of saliva is a necessity that is hard to 'schedule' in between generating limb command signals. However, the EMGs themselves can be used as a command signal that is even larger in nature than the EEG signal itself. Because random EMG activities over the motor areas naturally occur and are hard to prevent, they may not make sense as a continuous proportional command signal. However, distinct patterns in the EMG can be effectively used as a discrete command signal if the EMG pattern generated as a command is distinct from that which occurs during the course of normal activities. We have tested the ability to detect a rapid double jaw clench from EEG electrodes placed over the motor cortices, and differentiate it from normal chewing, swallowing, and talking activities. We have been able to get 100% correct classification using linear combinations of the RMS EMGs over a moving time series of windows. We are now working to adjust the number, width, and distance apart of these windows to generate robust classification of willful double jaw clicks against a wider range of chewing and swallowing activities.

The ability to use these EMGs in conjunction with EEGs is dependent on the ability to separate out the low amplitude EEG from the EMG before decoding of the EEG signals. Surface EMGs contain a range of frequencies that include the EEG range at the low end and peak at 100 Hz or more. Since non-invasive EEGs do not contain frequencies in the 100 Hz range, the frequency content of the signal at or near 100 Hz can potentially be used to estimate the EMG contamination in the lower EEG ranges. We investigated how well frequency amplitude in the 100 Hz range predicted the amplitude in the 12 Hz range during intentional EMG artifact generation, and found a clear linear relationship that can potentially be exploited to remove EMG artifacts in the EEG range (see Figure 27). It appears that a simple linear correction function can be used to remove EMG contributions. We are now investigating the effect of this removal function on the overall quality of EEG control. If EMG can be successfully removed with little or no degradation of the EEG signal, this will allow us to combine the EEG continuous commands with the EMG-based discrete commands while also eliminating effects of naturally occurring EMG activity.

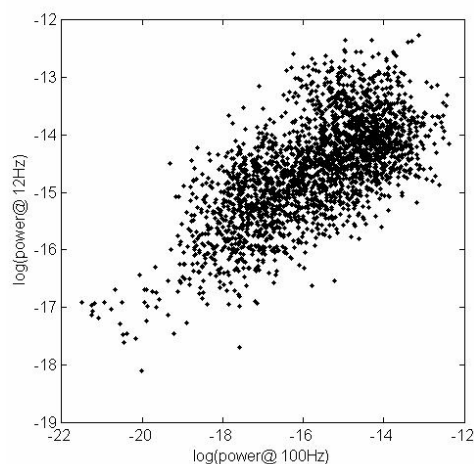


Figure 27. EMG contamination in the EEG range as a function of EMG content in a non-EEG range (i.e. 100Hz). This relationship can be used to identify and subtract out EMG contamination in the EEG-based command signal.

References

Taylor, D.M., S.I.H. Tillery, and A.B. Schwartz, Direct cortical control of 3D neuroprosthetic devices. *Science*, 296: p. 1829-1832, 2002.

Wolpaw, J.R. and D.J. McFarland, Control of a two-dimensional movement signal by a non-invasive brain-computer interface in humans. *Proceedings of the National Academy of Sciences of the United States of America*, 101(51): p. 17849-17854, 2004.